Ultra-Wide Range Pressure Sensor based on Microstructured Conductive Nanocomposite for Wearable Workout Monitoring

*Yongrok Jeong†, Jimin Gu†, Jaiyeul Byun, Junseong Ahn, Jaebum Byun, Kyuyoung Kim, Jaeho Park, Jiwoo Ko, Jun-ho Jeong, Morteza Amjadi, and Inkyu Park**

Yongrok Jeong, Jimin Gu, Junseong Ahn, Dr. Kyuyoung Kim, Dr. Jaeho Park, Jiwoo Ko, Prof. Inkyu Park
Department of Mechanical Engineering, Korea Advanced Institute of Science and Technology, 91, Daehak-ro, Yuseong-gu, Daejeon, 34141, Republic of Korea
E-mail: inkyu@kaist.ac.kr

Yongrok Jeong, Junseong Ahn, Jiwoo Ko, Dr. Jun-ho Jeong
Department of Nano-manufacturing Technology, Korea Institute of Machinery and Materials, 156, Gajeongbuk-ro, Yuseong-gu, Daejeon, 34103, Republic of Korea

Jaiyeul Byun, Jaebum Byun
Bros PT Lab,
4, Mannyeonnam-ro 3beon-gil, Seo-gu, Daejeon, 35200, Republic of Korea

Dr. Morteza Amjadi
Institute of Mechanical, Process and Energy Engineering, Heriot-Watt University, Edinburgh EH14 4AS, UK

Keywords: resistive pressure sensor, contact resistance, wide pressure range, healthcare pressure, workout pressure

Abstract

Conventional flexible pressure sensors are not suitable for the high-pressure applications due to their low saturation pressure. In this study, an ultra-wide range pressure sensor is designed based on the optimized microstructure of the carbon nanotubes-polyimide nanocomposite film. The sensing range of the pressure sensor is expanded by adopting polyimide with a high elastic modulus as a matrix material and its sensitivity is improved through functional sensing film with tip-flattened microdome arrays. As a result, the pressure sensor can measure a wide pressure range (0 kPa ~ 3000 kPa) and possesses the sensitivity of 5.66×10^{-3} ~ 0.23×10^{-3} kPa^{-1} with high reliability and durability up to 1,000 cycles. The proposed sensor is integrated into the hand and foot pressure monitoring systems for workout monitoring. The representative values of the pressure distribution in the hands and feet during the powerlifting are acquired and analyzed through Pearson's correlation coefficient. The analyzed results suggest that the pressure sensor can provide useful real-time information for healthcare and sport performance monitoring.

1. Introduction

Flexible and wearable pressure sensors are being extensively studied for various applications including electronic skins,[1–3] soft robotics,[4–7] healthcare monitoring,[8–12] and energy harvesting.[13] Among different sensing mechanisms of flexible pressure sensors (*e.g.*, capacitive, optical, piezoelectric, and triboelectric), contact-resistance type pressure sensors have been actively explored due to their simplicity, low fabrication cost, and high adaptability.[14,15] These types of pressure sensors basically measure the external pressure via changes in the contact resistance induced by the mechanical deformation of the functional sensing film, meaning that saturation of the structural deformation of the sensing film dramatically limits the pressure sensing capability of flexible pressure sensors.

Soft materials such as polydimethylsiloxane and Ecoflex are typically utilized for the fabrication of flexible pressure sensors thanks to their low elastic modulus, high stretchability, and human-friendliness[10,13,16–18]. However, these elastomers suffer from structural saturation at low pressures, making their use challenging in applications that involve high pressures.[19]Additionally, it is highly desirable to fabricate flexible pressure sensors in planar thin film type, which can lead to high adaptability to be attached onto surfaces with complex shapes as an add-on component.[10,13,20] However, the low elastic modulus of soft materials may cause handling problems, especially when the thickness of sensors is small.

Development of pressure sensors from thin polymeric films with a high elastic modulus can overcome the aforementioned limitations, while the high elastic modulus can inhibit the structural deformation at the same time, which may decrease the sensitivity of pressure sensors. To improve the sensitivity, microstructuring (*e.g.*, pyramidal shape) of the functional film has been recently suggested as an effective approach.[11,14,21,22] However, microstructuring of the

sensing film decreases the pressure sensing range of flexible sensors due to the stress concentration.[11,22,23] Therefore, there is always a trade-off relationship between sensitivity and sensing range, and it is essential to optimize the structure of the sensing film for specific applications.

Herein, we propose an ultra-wide range pressure sensor based on the polyimide/carbon nanotube (PI/CNT) functional film with an optimized tip-flattened microdome shape (**Figure 1a**), and integrate it into the workout monitoring system (Figure 1b). The pressure sensitivity originates from the change in the contact resistance at the interface of the PI/CNT functional film and an electrode film (Figure 1c). To maximize the pressure sensing range, a tip-flattened microdome shaped structure was selected and optimized by numerical simulation. Based on the optimization, the pressure sensor was fabricated and characterized. Since the polyimide (PI), which has a high elastic modulus, was adopted as the matrix material, our sensor can have a wide pressure sensing range (0 ~ 3000 kPa). Furthermore, it exhibits a fast response time (< 0.3 s at 3000 kPa) and reliable response to more than 1000 repeated loading cycles. The designed pressure sensor was integrated into shoes and pads for the monitoring of the pressure in the hands and feet. Through the acquired data from the proposed system, dynamic changes in the body pressure signals (*e.g.* heartbeat, pull-up, gait cycle) were successfully monitored, and the balance of the body movements was analyzed during powerlifting *via* Pearson's correlation coefficient (PCC). Although this research mainly focused on the powerlifting monitoring to show the practical usage of ultra-wide pressure range, the same strategy can be applied in the rehabilitation test, such as the rehabilitation of the stroke patients, because of its usefulness in the balance monitoring.[24,25]

2. Results and Discussion

2.1. Sensing Principle and Fabrication

The pressure sensor is composed of two parts: electrode film and microstructured PI/CNT film (**Figure 1a**). The amplitude of pressure is measured through changes of the contact resistance between the electrode and the PI/CNT functional film. When the pressure is applied to the PI/CNT film, the microscopic deformation of the PI/CNT film leads to changes in the contact area and the contact resistance between the electrode and PI/CNT film as well (Figure 1c-i). The contact resistance of the sensor upon application of an external force can be calculated as below:[26–28]

$$\mathrm{R_c} = \sqrt{\frac{\rho^2 \eta \pi H}{4\mathrm{F}}} \quad (1)$$

where $\mathrm{R_c}$ is the contact resistance, ρ is the resistivity of the contacted material, η is the empirical coefficient of order unity, H is the hardness of the contacted material, and F is the contact force. The above equation can be rewritten as the following equation:[27]

$$\log \mathrm{P} = k \log \frac{\mathrm{G}}{G_0} \quad (2)$$

where k is an empirical constant, G is the conductivity of the PI/CNT film under pressure (P), and $\mathrm{G_0}$ is the initial conductivity of the PI/CNT film without pressure. According to the equation, k value can be calibrated and the level of the applied pressure can be measured as a function of the conductance change.

The electrode film was initially fabricated by the deposition of 200 nm thick gold (Au) on a patterned PI film and subsequent lift-off process (see Experimental Section for details). For the fabrication of the microstructured PI/CNT film, a silicon mold was first created by RIE etching with chrome masking (Figure S1a). Next, the CNT dispersed solution was spray coated over

the silicon mold, and the PI varnish was cast onto the CNT coated mold (Figure S1b). The microstructured PI film with the embedded CNT network was then peeled-off from the mold after the baking process. The fabrication of the sensor was finally completed by assembling the microstructured PI/CNT film on the electrode by a Kapton tape. The overall thickness of the pressure sensor was around 158.6 μm (21 μm electrode film, 27.6 μm microstructured PI/CNT, and 110 μm Kapton tape) (Figure 1c-ii). Its thickness can be further reduced by replacing the Kapton tape with a thinner one.

2.2 Optimization of Tip flattened Microdome Structure

Prior to the fabrication of the pressure sensor, we ran a series of finite element method (FEM) simulations to optimize the topology of the PI/CNT sensing film. The powerlifting involves the heaviest weights among various workout activities. If the designed sensor endures the whole powerlifting, it can safely measure the pressure range of almost all types of workout. Powerlifting is composed of three movements: bench press, deadlift, and squat. Among them, the highest pressure is applied to the hand during the deadlift due to the small contact area and high weight. To date, the world record of the deadlift is 501 kg,[29] and the contact area of the barbell and hand can be calculated as 1.65×10^{-3} m^2 (**Figure S2a**). Consequently, the pressure applied to the hand can be calculated as 3000 kPa (Figure S2b). Accordingly, we set the target pressure range of our sensor to 0 ~ 3000 kPa.

In the tip-flattened microdome structure, two factors mainly govern the structural deformation: the density of the array and shape of the pattern. In the case of the array, the tip-flattened microdome was arranged hexagonally with a high packing ratio (~ 91 %), ensuring a uniform contact between PI/CNT film and electrode. It is proved to be the maximum achievable packing ratio according to the Thue's theorem.[30] The tip of microdome structure needs to be flattened

in order to reduce the stress concentration below the yield strength of PI. However, the flattening increases the initial contact area and conductivity, which in turn can decrease the overall sensitivity of the sensor. Therefore, the tip flattening of the microdome has a trade-off effect on the measurable pressure range and sensitivity.

The simulation was conducted with a unit cell structure of the hexagonal tip-flattened microdome pattern (**Figure S3**). The normalized contact area was calculated against various h/r ratio of the designed pattern, where h and r are the height of the pattern and the radius of flattened area, respectively (**Figure 2a**). As expected, higher h/r value, which can be interpreted as the smaller flattened area because of the closely packed array, brings higher sensitivity to the sensor. The von Mises stress of the tip-flattened microdome versus h/r values was further computed under a uniform applied pressure of 3000 kPa (Figure 2b). As shown in the figure, the maximum von Mises stress exceeds the yield strength of PI (69 MPa at 23 ℃ [31]) when the h/r value is higher than 3.

According to our simulation, the tip-flattened microdome with the optimized h/r of 3 was selected for the construction of the pressure sensor. The RIE etching process was adopted for the fabrication of the mold. The r value was controlled through the pattern of the initial mask and the h value was tuned by the RIE etching depth. As shown in Figure 2c, the target microstructure was achieved by 30 min of RIE. Over 35 min of etching, the patterns contacted each other, which collapsed the silicon mold by the following PI/CNT molding process.

With the optimized mold, the microstructured PI/CNT film was successfully fabricated by molding/demolding process (Figure 2d). Figure 2e depicts the cross-sectional SEM image of the microdome structure, revealing respective r and h values of 3.2 and 9.6 μm, which is similar

to the optimized morphology (h/r = 3). In order to confirm the successful transfer of the CNT thin film to the PI film, the PI/CNT film was intentionally torn and cross-sectional SEM images were taken, showing that PI fully penetrated into the porous CNT network and a CNT film with a thickness of about 1 μm was embedded on the top surface of the PI film (**Figure S4**).

2.3. Characterization of Pressure Sensor

Additional experiments were carried out to evaluate the electromechanical performance of the fabricated pressure sensor. The static/dynamic electromechanical tests were conducted through a custom-made tensile tester (**Figure S5a**), and the reliability test was performed by an ultimate tensile strength (UTS) tensile tester (Figure S5b). The sensitivity was defined as $d(G/G_0)/dP$. **Figure 3a** illustrates the response of a sensor under quasi-static pressures ranging from 0 to 3000 kPa with a deformation speed of 1 μm/s. The sensor demonstrated the maximum sensitivity of 5.66×10^{-3} kPa^{-1} at 50 kPa and the minimum sensitivity of 0.23×10^{-3} kPa^{-1} at 3000 kPa. Figure 3b shows the sensor response in log-log scale, revealing a nonlinear behavior for pressures up to 100 kPa. This can be explained by the partial surface wrinkling of the sensor or dust trapping between the electrode film and PI/CNT film during our lab-scale manufacturing, which can cause an unintentional change in the initial contact resistance. In contrast, the sensor showed a linear response ($R^2 = 0.996$) to pressures over 100 kPa due to the conformal contacts between the electrode and the PI/CNT film. The dynamic response of a sensor to the stepwise pressure loading-unloading is shown in Figure 3c and 3d. The sensor responded to all pressure levels (*i.e.*, 10 kPa, 30 kPa, 100 kPa, 300 kPa, 1000 kPa, and 3000 kPa) with high sensitivity and stability. The output signal of the sensor was identical at each loading stage. The reliability of a sensor was further examined under 1,000 repeated cycles of the pressure loading from 100 kPa to 3000 kPa, showing no significant change (*e.g.*, fluctuation or drift) in the sensor response (Figure 3e). This indicates that the response of the sensor is highly reliable under dynamic

loading and there is no significant permanent deformation in the PI/CNT film for pressure as high as 3000 kPa. To the best of our knowledge, our sensor showed the widest pressure range among the flexible pressure sensors that have been reported to date.

2.4. Application in Workout Pressure Monitoring

2.4.1. Details of Workout Pressure Monitoring System

As explained in the experiments above, our pressure sensor can measure an ultrawide range of pressures with a high sensitivity since the high modulus of the PI matrix and optimized microstructure allow for both low- and high-pressure sensing applications. For minute pressure sensing, a sensor was attached onto the wrist in the radial artery (Figure 4a, left) and its output signal was continuously measured in the rest mode and after squat exercise. (~15 kPa[32]). The acquired pulse rates in the rest state and after workout were about 72 and 114 bpm, respectively, showing significant increase of the pulse rate after exercise (Figure 4a). Notably, the sensor was able to distinguish both systolic and diastolic peaks of the arterial pulse waveform.[33] These experiments highlight the high sensitivity of the microstructured pressure sensor for detecting pressures less than 15 kPa.

The physical interaction of humans with the external environment is performed by their terminals: hands and feet. Real-time pressure monitoring of these terminals during workout can provide useful information regarding athletes' performance and health status. In order to monitor the hand pressure, we built a hand pressure monitoring system composed of two sensors: H1 sensor to monitor the pressure of the inner proximal phalange (2^{nd} proximal phalange), and H2 sensor to record the pressure of either outer proximal phalange (5^{th} proximal phalange) or hypothenar (Figure 4b, left, and **Figure S7a**). Specific regions for inner proximal phalange and outer proximal phalange are illustrated in Figure S2, and the raw data of each

sensors can be found in **Figure S8**. For instance, in the case of the pull-up movements (pressure ~300 kPa) (Figure S2c), H1 and H2 sensors monitor the inner and outer proximal phalange pressures, respectively. The sensors showed a large signal deviation in quick pull-up motions, which are often accompanied by high dynamic forces. Conversely, they produced small signal changes in the case of slow pull-up movements, showing generation of low dynamic forces (Figure 4b, right). The signal of the sensors remained stable during holding motion, demonstrating that static-like pressure was applied to them. Our results are consistent with previous findings,[34] confirming that the hand pressure monitoring system operated well for monitoring pressure levels in the range of hundreds of kPa.

To monitor the foot pressure, three pressure sensors were integrated under the shoe outsole (Figure S7b). F1 and F2 sensors measure the pressure of inner (first toe side) and outer (little toe side) metatarsal, respectively. The F3 sensor monitors the pressure of the heel (Figure 4c, left). The raw data of each sensors can be found in Figure S8. The pressure monitoring system was utilized in the human gait pattern monitoring where the amplitude of pressure can be around ~300 kPa.[35] The first step of the left foot showed sensor peak movement from FL3 (the heel of the left foot) to FL1 and FL2 (metatarsal of the left foot) and similar change of pressure is observed in the following step of the right foot (Figure 4c, right). In addition, the peak of FR3 occurred after the peaks of FL1 and FL2, which reflects the alternating landing motions of two feet in the human gait. These experimental results confirm that the analyzed pattern through this system is identical to the conventional study of the gait cycle.[36,37]

2.4.2. Application in Powerlifting Pressure Monitoring

Powerlifting is one of the most popular strength sports. Since it involves heavy weights, the balance between the left and right sides of the body is one of the most important factors for optimal workout performance. The unbalanced pressure distribution can cause skeletal damage

and even serious injuries. Thus, the real-time balance monitoring can improve the workout performance and prevent injuries. We used our pressure monitoring system to track the body balance during the powerlifting. For the quantitative comparison, the Pearson's correlation coefficient (PCC) was calculated to evaluate the mutual relationship between the left and right sides of the body.[38] The PCC is defined as follows:

$$r_{xy} = \frac{\sum_{i=1}^{n}(x_i-\bar{x})(y_i-\bar{y})}{\sqrt{\sum_{i=1}^{n}(x_i-\bar{x})^2}\sqrt{\sum_{i=1}^{n}(y_i-\bar{y})^2}} = \frac{Covariance\ between\ x,y}{Variance\ of\ x \times Variance\ of\ y} \quad (3)$$

where n is the sample size, x_i, y_i are the i^{th} points for x and y, and $\bar{x}$, $\bar{y}$ are the averages of x and y values, respectively. PCC equal to 1 denotes the perfect positive correlation, while PCC closed to 0 shows no correlation between x and y, and PCC equal to -1 represents the perfect negative correlation. We monitored all typical motions of the powerlifting (*i.e.*, bench press, squat, deadlift) with correct and wrong poses (frequent mistakes of novice). Examples of the wrong pose include imbalance between left and right hands, a perturbation between right and left feet leading to unstable dynamics, and pelvic deflection that causes imbalance in hand and foot motions. The results of our pressure monitoring system were studied and confirmed by a National Strength and Conditioning Association (NSCA) certified personal trainer. For each motion, the interest regions were encircled with red dot line for clarity (**Figure 5a**).

Prior to PCC evaluation, the system was validated by analyzing the sample dynamic movements. For example, in the squat exercise (Figure 5b), the human body undergoes repeated cycles of upward and downward movements and thus abrupt pressure changes occur on feet when the direction of the motion is changed. This can be clearly observed in plots for the correct pose in Figure 5b: valleys/peaks amid each repeat. In addition, movement in the center of pressure (COP) can be analyzed. In biomechanics, COP is the area-averaged point of the ground reaction force (GRF) which denotes the force between feet and ground. Since COP is one of the most important terms to analyze the balance of the human body, analyzing the movement of COP is

important. The same example shows that the pressure increased in metatarsal (F1, F2) and decreased in heel (F3) with the squat-down motion, while an opposite trend was observed in the case of the stand-up motion. Because the metatarsal area is placed forward part of the foot and the heel area is placed backward part of the foot, this pressure tendency can be interpreted as the COP movement in forward/backward directions during the workout.

Next, the workout was analyzed through the PCC evaluation (Figure 5b). In the case of the squat (Figure 5b-i, **Figure S9a**), the pressure variations were dominant in the feet. The PCC values were 0.77 ± 0.15 (F1) / 0.83 ± 0.14 (F2) / 0.73 ± 0.08 (F3) for the correct pose (**Movie S1**), and -0.19 ± 0.22 (F1) / -0.56 ± 0.09 (F2) / 0.43 ± 0.41 (F3) for the wrong pose (**Movie S2**). In the case of the bench press (Figure 5c-ii, Figure S9b), a considerable pressure change was noticed in the hand. The PCC values were calculated as 0.87 ± 0.06 (H1) / 0.91 ± 0.02 (H2) for the correct pose (**Movie S3**), and 0.68 ± 0.19 (H1) / 0.76 ± 0.07 (H2) for the wrong pose (**Movie S4**). In the case of the deadlift (Figure 5c-iii, Figure S9c), both hands and feet experienced changes in the pressure distribution. The PCC values were 0.50 ± 0.23 (H1) / 0.79 ± 0.08 (H2) / 0.77 ± 0.08 (F1) / 0.76 ± 0.10 (F2) / 0.82 ± 0.03 (F3) for the correct pose (**Movie S5**), and 0.20 ± 0.29 (H1) / 0.32 ± 0.0.53 (H2) / 0.47 ± 0.13 (F1) / 0.63 ± 0.12 (F2) / 0.67 ± 0.21 (F3) for the wrong pose (**Movie S6**). From the above analyses, PCC values in the correct pose always remained higher than those of the wrong pose. This difference possibly originated from two factors: permanent imbalance and temporary imbalance. The response of the H2 sensor between 2 – 4 s during the bench press with a wrong pose, is a good example of the permanent imbalance. Since the force was concentrated on the left-hand, the pressure variation was much less in the right-hand. This causes a nonlinear tendency between changes of pressure in left and right hands, resulting in a decrease in the PCC value. The signal of the F2 sensor within 3 – 4 s during the squat with the wrong pose is particularly a good example of the temporary imbalance. When the performer loses the balance, perturbation of the pressure in between left and right feet with

the opposite pressure change tendency was observed for the balance restoration. This dramatically decreases the PCC even to a negative value. The deadlift shows both permanent and temporary imbalances. For example, the response of the F1 sensor in 10 – 12 s showed a permanent imbalance, while the response of the H2 sensor between 4 – 6 s depicted a temporary imbalance. These results highlight the potential application of our pressure monitoring devices in real-time sport performance monitoring. Compared to previously developed complex and expensive methods of the body balance monitoring through force plates and 3D motion capture,[39–42] our pressure monitoring systems can analyze the sign of instability in a quantitative, personalized, and cost-effective manner.

3. Conclusion

In summary, a high-performance pressure sensor capable of sensitive measurement of ultrawide range pressures (0~3000 kPa) was developed through the optimization of tip-end flattened microdome arrays. The working mechanism of the pressure sensor is based on the change in the contact resistance between microstructured PI/CNT and electrode film. In order to cover the wide target pressure range (0~ 3000 kPa), tip-end flattened microdome shaped structure was adopted, and the degree of flattening was optimized through the FEM simulation. The sensor showed a stable and reliable response to cyclic pressure loading. As practical applications of the developed sensor, it was successfully used to monitor various body pressures ranging from wrist pulse pressure (~15 kPa) to gait pressure (~300 kPa), and pull-up pressure (~300 kPa). In addition, the integrated pressure monitoring system showed potential in balance monitoring during the powerlifting via PCC analysis. Even though the powerlifting was adopted to show both the practical usage of the ultra-wide pressure range and the availability of balance monitoring through PCC analysis, the same strategy can be applied to the rehabilitation test, such as the gait rehabilitation test of the stroke patient, because it can be applied in every case that needs to observe the balance of human body. Furthermore, we envision that the proposed pressure sensor can be utilized in various applications including healthcare monitoring and sports performance monitoring, where conventional flexible pressure sensors cannot function due to their limited pressure measurement ranges.

4. Experimental Methods

Materials: PI (PI-1388) was purchased from Vtec (USA). CNTs were purchased from Hanhwa Chemical, South Korea. The polymer for anti-fouling coating (Soilnon AF-20) was purchased from Nicca Korea (South Korea). Before usage, it was diluted in the Novec 7100 Engineering fluid from 3M with a ratio of 1 wt%.

Fabrication of Electrode Film: The PI solution was spin coated (3000 rpm, 30 s) on a 4 inch silicon (Si) wafer and baked (oven baking of 1 hr at 150 ℃ and 4 hr at 260 ℃) to form the substrate layer. The photolithography process was used to pattern the AZ5214E photoresist (PR) on the PI film. In the case of the reversal baking process of the PR, since the temperature of the PR layer was affected by the PI layer, only the post exposure baking (PEB) temperature was changed from 120 ℃ to 122.5 ℃, and other conditions remained same compared with the suggested recipe. The electrode layer (titanium (Ti) 30 nm for adhesion / gold (Au) 200 nm for conductance) was then deposited the PR layer through the electron beam evaporator (E-beam evaporator). The deposited film was patterned through the PR development and lift-off process. Except for the regions to be connected with the PI/CNT film and flexible printed circuit (FPC) connector, an additional PI layer was formed for the insulation with aforementioned condition. Masking for the selected region was made simply by attaching the Kapton tape before the spin coating process.

Fabrication of Tip-flattened Microdome Shaped Mold: The LOR resist was initially coated (PMGI SF9, spin coated for 30 s at 5000 rpm, and baked on a hot plate for 5 mins at 190 ℃) on a 4-inch Si wafer followed by PR coating (AZ5214E, spin coated for 30s at 3000 rpm, and

baked for 1 min at 110 ℃) (Figure S1a-i). The coated PR layer was then patterned through the conventional positive lithography process. The PMGI SF9 layer was patterned with the same etchant of the AZ5214E (AZ 300 MIF) for 30 s. On the patterned layer, 300 nm of Chrome (Cr) was deposited by the E-beam evaporator and patterned by the lift-off process (Figure S1a-ii). Patterned Cr was used as the mask for the following RIE process with a condition as following: Working pressure of 150 mmHg, power of 50 W, and gas flow of SF_6 20 sccm for 30 min (Figure S1a-iii). Next, the Cr mask was stripped by CR-7 etchant (Figure S1a-iv).

Fabrication of PI/CNT Functional Film: On the structured Si mold, anti-fouling coating (AF coating) was conducted by soaking the mold into the diluted Soilnon AF-20 solution for 1 hr. 60 mL of the CNT/IPA diluted solution with a ratio of 0.05 wt%, mixed *via* tip sonicator (VCX130, Sonics & Materials Inc., USA) for 1 hr, was spray coated on the AF coated Si mold heated by a hot plate at 150 ℃ (Figure S1b-i). The spray coated CNT layer was covered with the PI solution by the spin coating at 1000 rpm for 30s (Figure S1b-ii). The formed PI film was then kept under vacuum for 10 min to remove the trapped air bubbles and subsequently and baked as before (Figure S1b-iii). Molded PI/CNT functional film was finally detached from the mold and assembled on the electrode film with the assist of a Kapton tape. The alignment of the PI/CNT film was performed through a bare eye (Figure S1b-iv).

Characterization of Pressure Sensing Performance: The pressure sensing was evaluated based on an experimental setup shown in Figure S5a. An SM-100 load cell (Interface Inc., USA) was used to measure the reference force value during the experiments. The force was applied by a linear actuator (Physik Instrumente GmBH & Co. KG, Germany). The motor speed of 1 and 50 μm/s was used for the static and dynamic pressure response tests, respectively. The reliability test was performed by a universal testing machine (AG-X plus series, Shimadzu, Japan) shown

in Figure S5b. The size of the tip was manufactured as the 15 mm X 15 mm. The test was conducted under base pressure of 100 kPa (22.5 N force) and upper limit pressure of 3000 kPa (675 N) with a speed of 50 μm/s.

Fabrication of Pressure Monitoring System: In order to reduce the disturbance possibly originated from the shear motion of the system, PET film with a thickness of 0.1 mm was laminated on both sides of the sensor before integration. In the case of the foot system, a space for the connector of each sensor (F1, F2, and F3) was retained by scraping out the top rubber pad partially. On the reserved space, the PET film laminated sensor was disposed of and covered with the bottom rubber pad. The whole system was fixed under the shoe outsole with bolts (Figure S7a). In the case of the hand system, laminated sensors (H1, H2) were sandwiched between two bottom and cover rubber pads *via* a double-sided tape. The cover rubber pad was wrapped on the surface of the barbell and fixed by a Velcro tape. Consequently, the sensor was placed between the barbell and cover rubber pad.

Experimental Details for Workout Pressure Monitoring: This experiment was approved by institutional review board of KAIST (IRB No. KH2021-006). The whole system used in the workout pressure monitoring is shown in Figure S5c, which is composed of power supply, data acquisition system (DAQ) from National Instruments (NI), and fabricated foot / hand pressure monitoring pads. Bench press was performed for 5 repeated cycles with the weight of 60 kg, and the pressure of the inner proximal phalange and the hypothenar were monitored through the system. Likewise, the squat was performed for 5 cycles with the weight of 60 kg, and the foot pressure of the metatarsals and heel were monitored through the food system. Deadlift was performed for 5 cycles with the weight of 70 kg, and both the foot pressure (metatarsals and heel) and the hand pressure (inner and outer proximal phalange) were monitored through the hand and foot system. For the analysis, to avoid any possible noise in the first and last cycles

due to the dynamic loading and unloading motions, the 3 middle cycles were used for data interpretation.

Supporting Information
Supporting Information is available from the Wiley Online Library or from the author.

Acknowledgements
†Yongrok Jeong and Jimin Gu contributed equally this work.
This work was supported by the National Research Foundation of Korea (NRF) grant funded by the Korea government (MSIT) (No. 2018R1A2B2004910). This work was supported by the National Research Foundation of Korea (NRF) Grant funded by the Korean Government (MSIP) (No. 2015R1A5A1037668).

Received: ((will be filled in by the editorial staff))
Revised: ((will be filled in by the editorial staff))
Published online: ((will be filled in by the editorial staff))

References

[1] D. J. Lipomi, M. Vosgueritchian, B. C. K. Tee, S. L. Hellstrom, J. A. Lee, C. H. Fox, Z. Bao, *Nat. Nanotechnol.* **2011**, *6*, 788.

[2] C. Wang, D. Hwang, Z. Yu, K. Takei, J. Park, T. Chen, B. Ma, A. Javey, *Nat. Mater.* **2013**, *12*, 899.

[3] X. Tang, C. Wu, L. Gan, T. Zhang, T. Zhou, J. Huang, H. Wang, C. Xie, D. Zeng, *Small* **2019**, *15*, 1.

[4] M. Amjadi, M. Sitti, *Adv. Sci.* **2018**, *5*, DOI 10.1002/advs.201800239.

[5] M. Amjadi, M. Sitti, *ACS Nano* **2016**, *10*, 10202.

[6] T. G. Thuruthel, B. Shih, C. Laschi, M. T. Tolley, *Sci. Robot.* **2019**, *4*, DOI 10.1126/SCIROBOTICS.AAV1488.

[7] C. M. Boutry, M. Negre, M. Jorda, O. Vardoulis, A. Chortos, O. Khatib, Z. Bao, *Sci. Robot.* **2018**, *3*, eaau6914.

[8] J. Zhong, Y. Ma, Y. Song, Q. Zhong, Y. Chu, I. Karakurt, D. B. Bogy, L. Lin, *ACS Nano* **2019**, *13*, 7107.

[9] T. Q. Trung, N. E. Lee, *Adv. Mater.* **2016**, *28*, 4338.

[10] K. Kim, J. Choi, Y. Jeong, I. Cho, M. Kim, S. Kim, Y. Oh, I. Park, *Adv. Healthc. Mater.* **2019**, *8*, 1.

[11] C. M. Boutry, A. Nguyen, Q. O. Lawal, A. Chortos, S. Rondeau-Gagné, Z. Bao, *Adv. Mater.* **2015**, *27*, 6954.

[12] C. M. Boutry, L. Beker, Y. Kaizawa, C. Vassos, H. Tran, A. C. Hinckley, R. Pfattner, S. Niu, J. Li, J. Claverie, et al., *Nat. Biomed. Eng.* **2019**, *3*, 47.

[13] J. Choi, D. Kwon, B. Kim, K. Kang, J. Gu, J. Jo, K. Na, J. Ahn, D. Del Orbe, K. Kim, et al., *Nano Energy* **2020**, *74*, 104749.

[14] S. C. B. Mannsfeld, B. C. K. Tee, R. M. Stoltenberg, C. V. H. H. Chen, S. Barman, B. V. O. Muir, A. N. Sokolov, C. Reese, Z. Bao, *Nat. Mater.* **2010**, *9*, 859.

[15] L. Pan, A. Chortos, G. Yu, Y. Wang, S. Isaacson, R. Allen, Y. Shi, R. Dauskardt, Z. Bao, *Nat. Commun.* **2014**, *5*, DOI 10.1038/ncomms4002.

[16] J. Choi, D. Kwon, K. Kim, J. Park, D. Del Orbe, J. Gu, J. Ahn, I. Cho, Y. Jeong, Y. Oh, et al., *ACS Appl. Mater. Interfaces* **2020**, *12*, 1698.

[17] S. Kim, M. Amjadi, T. I. Lee, Y. Jeong, D. Kwon, M. S. Kim, K. Kim, T. S. Kim, Y. S. Oh, I. Park, *ACS Appl. Mater. Interfaces* **2019**, DOI 10.1021/acsami.9b07636.

[18] D. Kwon, T. I. Lee, J. Shim, S. Ryu, M. S. Kim, S. Kim, T. S. Kim, I. Park, *ACS Appl. Mater. Interfaces* **2016**, *8*, 16922.

[19] J. Lee, J. Park, H. Jeong, K. H. Shin, D. Lee, *J. Ind. Eng. Chem.* **2016**, *42*, 131.

[20] D. Lee, J. Kim, H. Kim, H. Heo, K. Park, Y. Lee, *Nanoscale* **2018**, *10*, 18812.

[21] L. Y. Chen, B. C. K. Tee, A. L. Chortos, G. Schwartz, V. Tse, D. J. Lipomi, H. S. P. Wong, M. V. McConnell, Z. Bao, *Nat. Commun.* **2014**, *5*, 1.

[22] S. H. Cho, S. W. Lee, S. Yu, H. Kim, S. Chang, D. Kang, I. Hwang, H. S. Kang, B. Jeong, E. H. Kim, et al., *ACS Appl. Mater. Interfaces* **2017**, *9*, 10128.

[23] Z. Huang, M. Gao, Z. Yan, T. Pan, S. A. Khan, Y. Zhang, H. Zhang, Y. Lin, *Sensors Actuators, A Phys.* **2017**, *266*, 345.

[24] J. W. Song, J. M. Kim, Y. S. Cheong, Y. S. Lee, S. M. Chun, Y. S. Min, T. Du Jung, *Ann. Rehabil. Med.* **2017**, *41*, 188.

[25] C. Arienti, S. G. Lazzarini, A. Pollock, S. Negrini, *PLoS One* **2019**, *14*, 1.

[26] R. S. Timsit, *IEEE Trans. Components Packag. Technol.* **1999**, *22*, 85.

[27] Y. Jeong, J. Park, J. Lee, K. Kim, I. Park, *ACS Sensors* **2020**, *5*, 481.

[28] S. C. B. Mannsfeld, B. C. K. Tee, R. M. Stoltenberg, C. V. H. H. Chen, S. Barman, B. V. O. Muir, A. N. Sokolov, C. Reese, Z. Bao, *Nat. Mater.* **2010**, *9*, 859.

[29] "Guinness World Record - Heaviest Deadlift," can be found under https://www.guinnessworldrecords.com/world-records/heaviest-deadlift, **2020**.

[30] H.-C. Chang, L.-C. Wang, *arXiv:1009.4322[math.MG]* **2010**, 1.

[31] Dupont, *DuPont Kapton HN Polyimide Film - Technical Datasheet*, Dover, NH, **2019**.

[32] Y. Zang, F. Zhang, D. Huang, X. Gao, C. A. Di, D. Zhu, *Nat. Commun.* **2015**, *6*, 1.

[33] M. F. O'Rourke, A. P. X. J. Jiang, *Br. J. Clin. Pharmacol.* **2001**, *51*, 507.

[34] J. A. I. Prinold, A. M. J. Bull, *J. Sci. Med. Sport* **2016**, *19*, 629.

[35] M. J. Hessert, M. Vyas, J. Leach, K. Hu, L. A. Lipsitz, V. Novak, *BMC Geriatr.* **2005**, *5*, 1.

[36] T. H. Hsieh, A. C. Tsai, C. W. Chang, K. H. Ho, W. L. Hsu, T. Te Lin, *Proc. Annu. Int. Conf. IEEE Eng. Med. Biol. Soc. EMBS* **2012**, 6772.

[37] W. Tao, T. Liu, R. Zheng, H. Feng, *Sensors* **2012**, *12*, 2255.

[38] P. W. Duncan, D. K. Weiner, J. Chandler, S. Studenski, *Journals Gerontol.* **1990**, *45*, 1.

[39] A. W. O. Gil, M. R. Oliveira, V. A. Coelho, C. E. Carvalho, D. C. Teixeira, R. A. da Silva Jr, *Brazilian J. Phys. Ther.* **2011**, *15*, 429.

[40] J. M. Leach, M. Mancini, R. J. Peterka, T. L. Hayes, F. B. Horak, *Sensors (Switzerland)* **2014**, *14*, 18244.

[41] A. N. P. Service, Wildlife, *Aust. ranger Bull.* **1986**, *4*, 9.

[42] C. Lou, C. Pang, C. Jing, S. Wang, X. He, X. Liu, L. Huang, F. Lin, X. Liu, H. Wang, *Sensors (Switzerland)* **2018**, *18*, DOI 10.3390/s18124193.

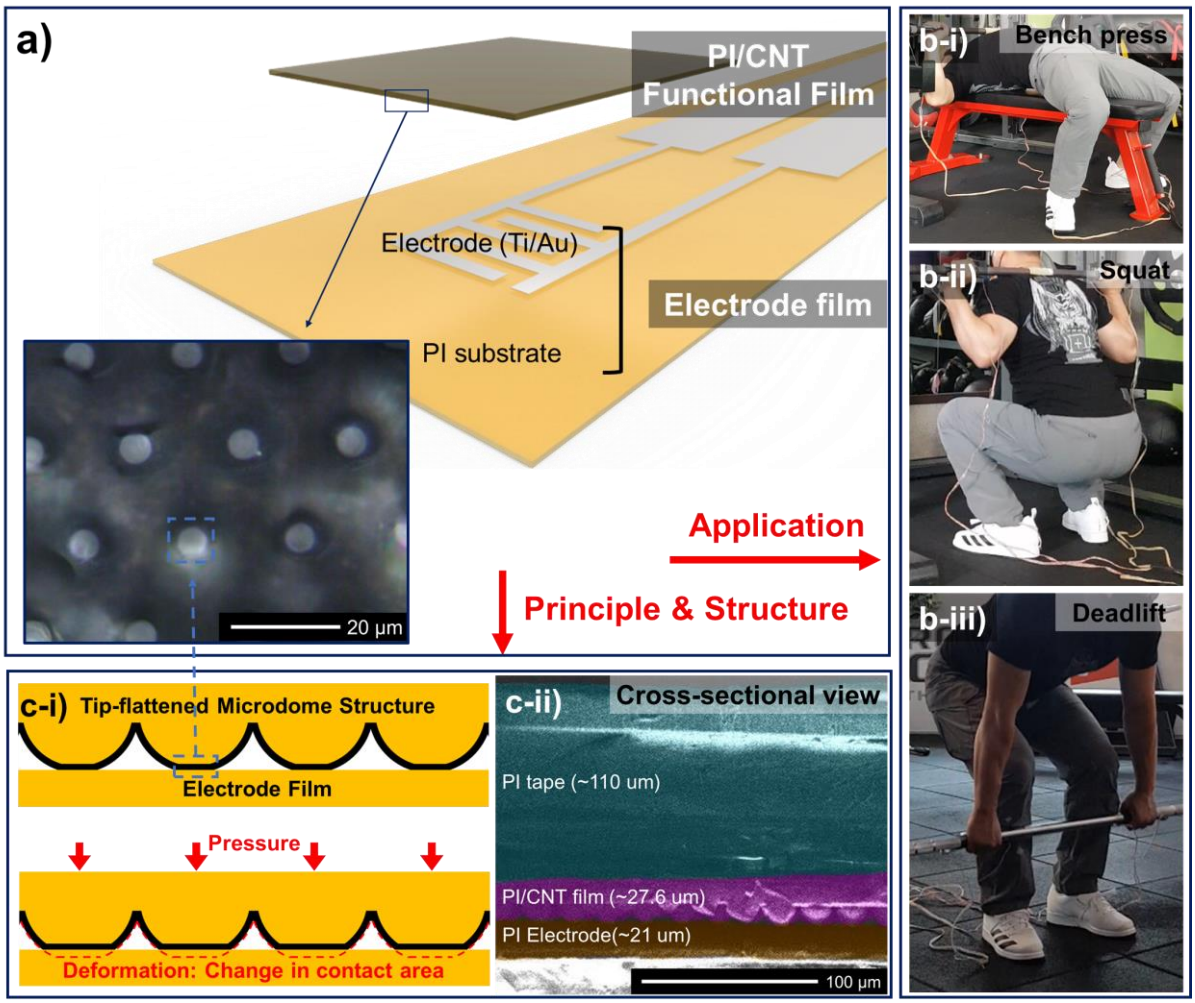

Figure 1. a) Schematic illustration of the proposed pressure sensor comprised of microstructured PI/CNT functional film and electrode film (inset: optical micrograph image focused on the flattened area); b) Application of the pressure in workout pressure monitoring. The hand and foot pressure monitoring under three workout exercises: bench press (i), squat (ii), and deadlift (iii); c) Sensing principle of the pressure sensor (i) and cross-sectional SEM image of the sensor (ii).

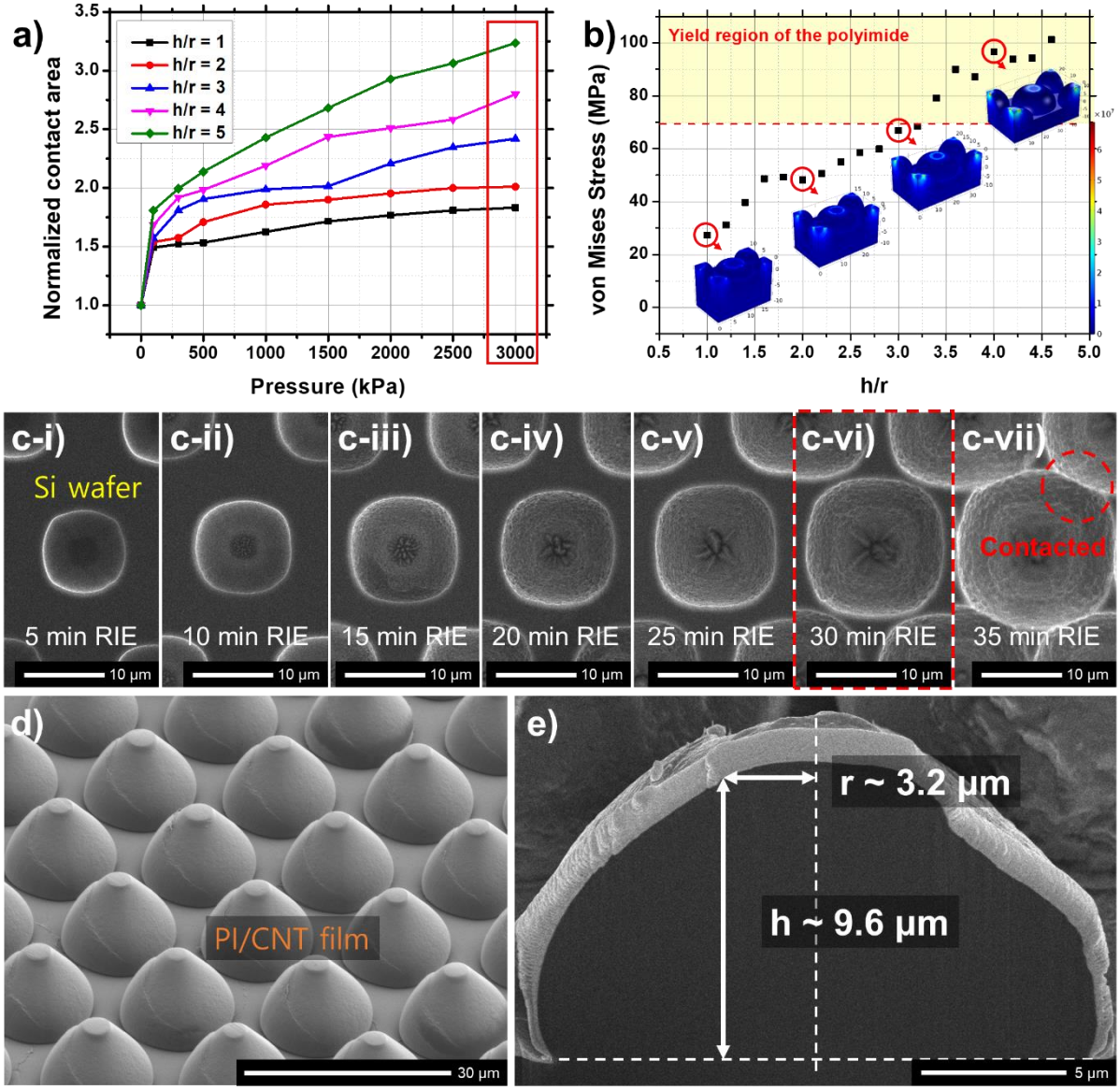

Figure 2. Optimization of the tip-flattened microdome structure for high-performance pressure sensing: a) Calculation of the normalized contact area against the applied pressure for various h/r ratios; b) Maximum von Mises stress of the cell versus h/r ratio upon a constant pressure of 3000 kPa; c) Optimization of the RIE process for the fabrication of the mold (Optimal RIE time ~ 30 min); d) SEM image of the fabricated PI/CNT film, showing tip-flattened microdome shapes; e) Cross-sectional SEM image of a tip-flattened microdome.

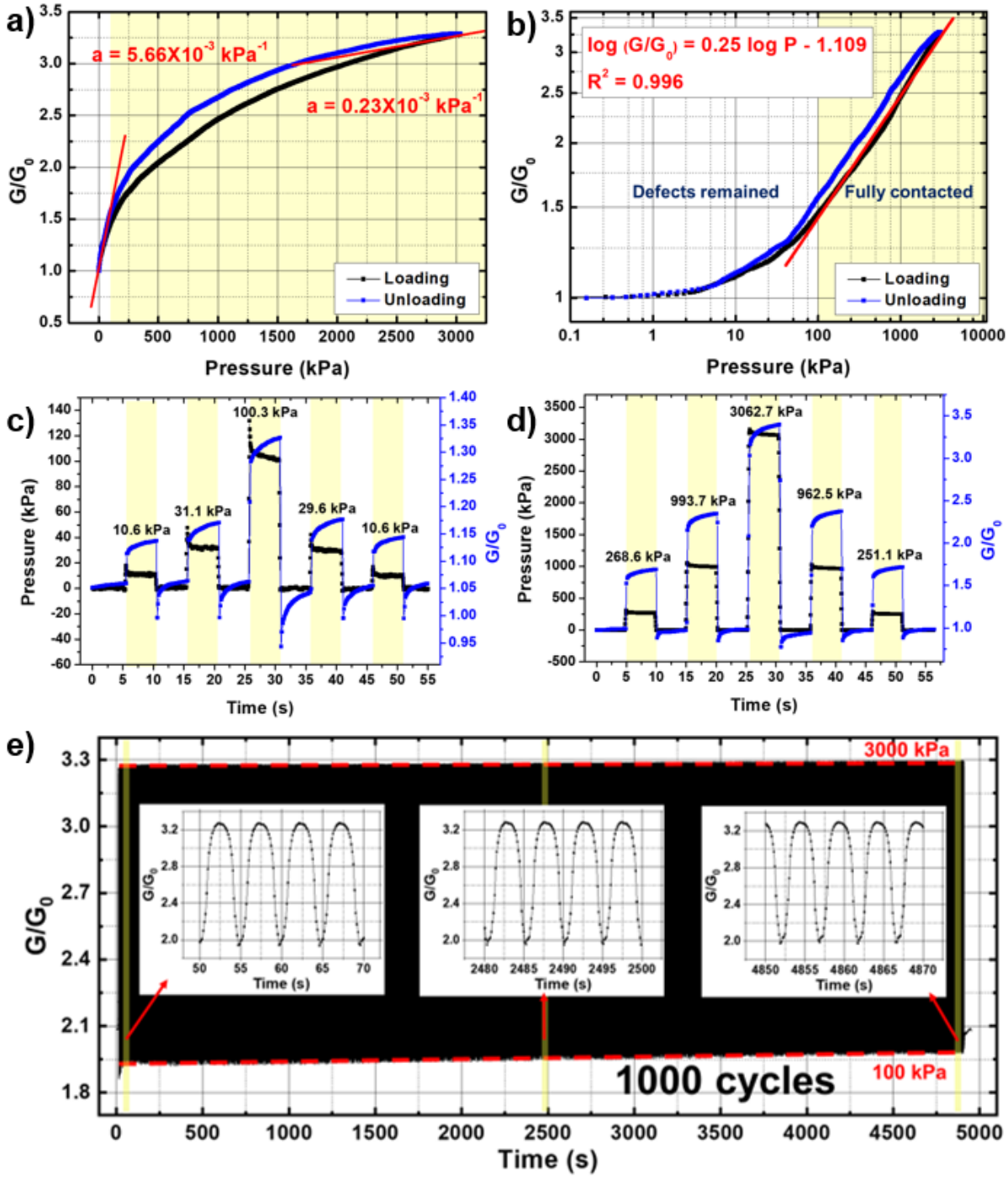

Figure 3. Pressure sensing performance of the pressure sensor: a) Result of the static pressure response test in a linear scale from 0 to 3000 kPa. The sensor showed sensitivity of 5.66×10^{-3} kPa^{-1} for the low-pressure regime and 0.23×10^{-3} kPa^{-1} for the high-pressure regime; b) Response of a sensor versus the applied pressure in log-log scale; c-d) Dynamic response of a sensor to stepwise pressure loading-unloading; e) Reliability of a pressure sensor under 1000 cycles of pressure from 100 kPa to 3000 kPa.

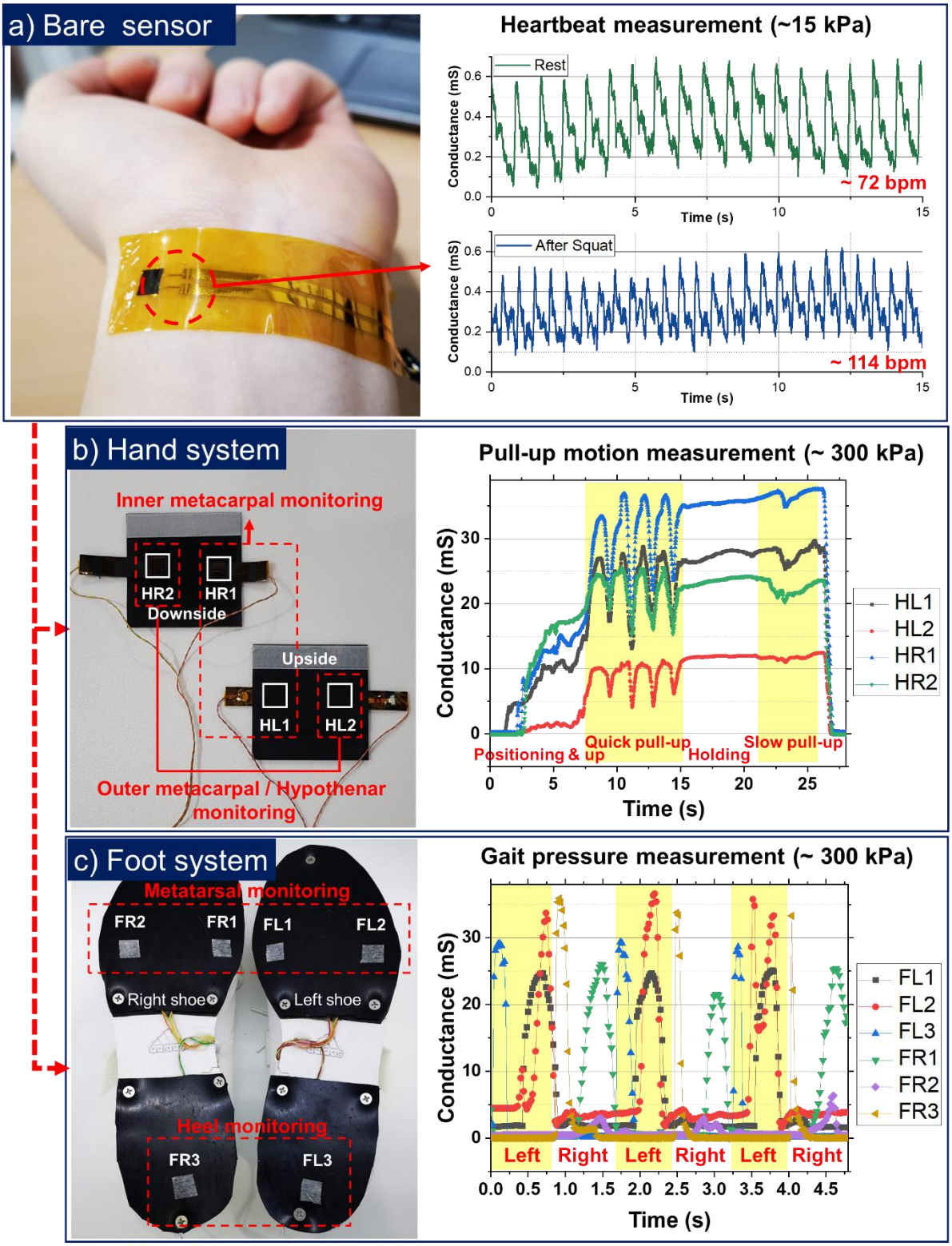

Figure 4. Applications of the pressure sensor: a) Output signal of a sensor when mounted on the wrist; b) Photograph of the hand pressure monitoring system composed of two integrated pressure sensors per hand (left). Response of the system to pull-up pressure (right); c) Photograph of the foot pressure monitoring system composed of three integrated pressure sensors per foot (left). Gait pressure monitoring using the foot monitoring systems (right).

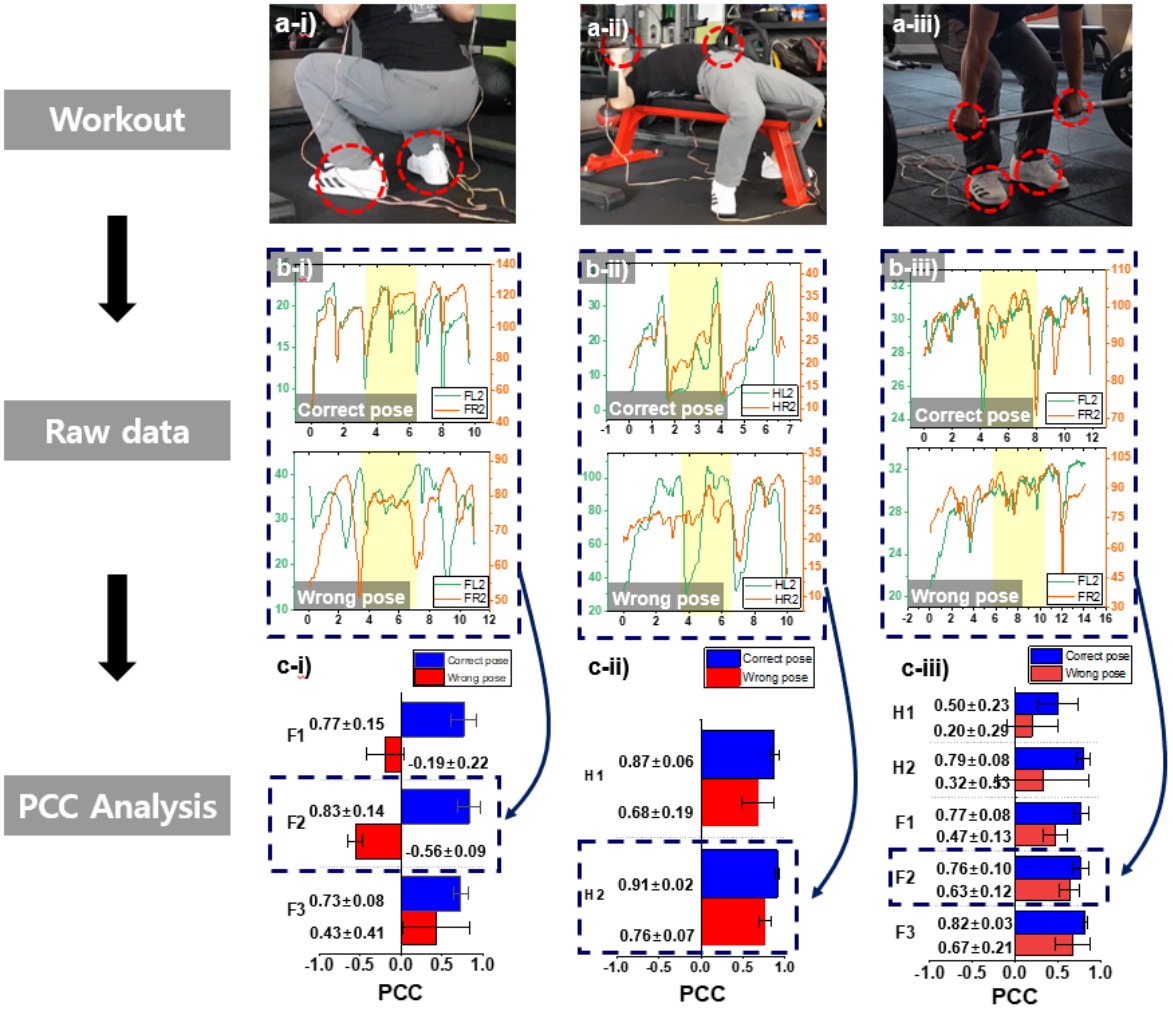

Figure 5. Analysis of the powerlifting pressure monitoring. a) Powerlifting experiments with the fabricated pressure monitoring system. The regions encircled by red dotted lines represent the mainly monitored regions for each workout; b) Example graphs for the raw data during workout (green: pressure of the left side, orange: pressure of the right side, x-axis: time). The upper graph is the result from the correct pose and the lower graph is the result from the wrong pose. Three cycles were repeated for each workout, and each cycle is divided by the yellow colored region in the plot. Raw data of measurement for every sensor can be found in Figure S9; c) PCC analysis results from the raw sensor responses. The region boxed with the blue dotted line was analyzed from the corresponding raw data in b).

A pressure sensor capable of ultrawide range of pressure sensing is developed based on an optimized microstructure. The pressure distribution of individuals' hand and foot during powerlifting is monitored through the fabricated sensor.

Keyword resistive pressure sensor, contact resistance, wide pressure range, healthcare pressure, workout pressure

*Yongrok Jeong†, Jimin Gu†, Jaiyul Byeon, Junseong Ahn, Jaibum Byeon, Kyuyoung Kim, Jaeho Park, Jiwoo Ko, Jun-ho Jeong, Morteza Amjadi, and Inkyu Park**

Ultra-Wide Range Pressure Sensor based on Microstructured Conductive Nanocomposite for Wearable Workout Monitoring